

Stretching and folding in finite time

Tian Ma, Nicholas T. Ouellette, and Erik M. Bollt

Citation: *Chaos* **26**, 023112 (2016); doi: 10.1063/1.4941256

View online: <http://dx.doi.org/10.1063/1.4941256>

View Table of Contents: <http://scitation.aip.org/content/aip/journal/chaos/26/2?ver=pdfcov>

Published by the AIP Publishing

Articles you may be interested in

[Large-deviation joint statistics of the finite-time Lyapunov spectrum in isotropic turbulence](#)

Phys. Fluids **27**, 085110 (2015); 10.1063/1.4928699

[Competitive autocatalytic reactions in chaotic flows with diffusion: Prediction using finite-time Lyapunov exponents](#)

Chaos **24**, 013109 (2014); 10.1063/1.4862153

[Transient chaos measurements using finite-time Lyapunov exponents](#)

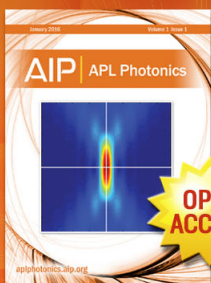
Chaos **20**, 033117 (2010); 10.1063/1.3483877

[Characterization of finite-time Lyapunov exponents and vectors in two-dimensional turbulence](#)

Chaos **12**, 688 (2002); 10.1063/1.1499395

[Geometrical constraints on finite-time Lyapunov exponents in two and three dimensions](#)

Chaos **11**, 16 (2001); 10.1063/1.1342079



Launching in 2016!

The future of applied photonics research is here

OPEN
ACCESS

AIP | APL
Photonics

Stretching and folding in finite time

Tian Ma,^{1,a)} Nicholas T. Ouellette,^{2,3} and Erik M. Bollt^{1,b)}

¹Department of Mathematics and Computer Science, Clarkson University, Potsdam, New York 13699, USA

²Department of Mechanical Engineering & Materials Science, Yale University, New Haven, Connecticut 06520, USA

³Department of Civil and Environmental Engineering, Stanford University, Stanford, California 94305, USA

(Received 22 July 2015; accepted 19 January 2016; published online 16 February 2016)

Complex flows mix efficiently, and this process can be understood by considering the stretching and folding of material volumes. Although many metrics have been devised to characterize stretching, fewer are able to capture folding in a quantitative way in spatiotemporally variable flows. Here, we extend our previous methods based on the finite-time curving of fluid-element trajectories to nonzero scales and show that this finite-scale finite-time curvature contains information about both stretching and folding. We compare this metric to the more commonly used finite-time Lyapunov exponent and illustrate our methods using experimental flow-field data from a quasi-two-dimensional laboratory flow. Our new analysis tools add to the growing set of Lagrangian methods for characterizing mixing in complex, aperiodic fluid flows. © 2016 AIP Publishing LLC. [<http://dx.doi.org/10.1063/1.4941256>]

One of the hallmarks of chaotic or turbulent fluid flows is rapid mixing. Vigorously stirred fluids mix so well because they move material quickly and yet are constrained to remain in a finite amount of space. The chaotic mixing process can thus be conceptualized as the result of *stretching*—that is, the rapid separation of nearby packets of fluid—and *folding*—that is, the bending of packets of fluid to maintain the overall volume. Because these two processes are fundamental for mixing, they have been the subject of intense study; however, many more methods have been developed to characterize stretching than folding. Here, we describe a method based on the propensity of the trajectories of fluid elements to curve that allows us to quantify both stretching and folding at the same time. We compare this technique with a more common tool that isolates only stretching and demonstrate our methods on data from an experimental flow.

I. INTRODUCTION

It is almost definitional to say that chaotic and turbulent flows mix efficiently: by a repeated process of stretching and folding material volumes,¹ chaotic advection² leads to mixing that is significantly enhanced relative to diffusion alone.³ Historically, this rapid mixing has been quantified and modeled using statistical metrics such as the relative dispersion of fluid elements⁴ or effective diffusivities.⁵ These kinds of tools capture the global effects of the fluid advection on mixing and can provide a simple, high-level parameterization of its effects that is useful for modeling.

But even though transport and mixing are sped up by chaotic advection on average, this enhancement is rarely uniform; rather, it mirrors the complex spatiotemporal

heterogeneity of the flow itself.⁶ Even in a flow that is in general strongly mixing, there may be regions that are separated from the rest of the flow by dynamical barriers, and which mix only weakly. In the terminology of dynamical-systems theory, these weakly mixing regions may be described as being elliptic, while those parts of the flow that mix strongly and transport material rapidly are hyperbolic. Since chaotic and turbulent flows are typically highly unsteady and aperiodic, however, the instantaneous elliptic or hyperbolic character of a particular region of the flow may change rapidly in time. Thus, any useful partitioning of the flow field into strongly and weakly mixing regions must identify not only places that are elliptic or hyperbolic but those that maintain their character over some macroscopic time window. Such regions may be said to be *coherent*⁷ and are often referred to as coherent structures.

Analyzing flows from the standpoint of coherent structures may allow us to move past global descriptions of transport and mixing, such as overall effective diffusivities or purely statistical models, to local characterizations. Such local information is often a very important complement to its global counterpart; in an oil spill in the ocean, for example, one is more interested in knowing which areas of the coastline will be affected than in the net spreading rate of the oil.^{8,9} Due to this goal, then, a vast set of methods has been devised to detect and characterize coherent structures in general unsteady flows. We focus here on methods that use primarily Lagrangian information; that is, techniques that are based on the information contained in the trajectories of fluid elements, typically computed over some finite time that specifies the window in which we desire coherence. Broadly, one can classify these methods into those that attempt to find the boundaries that separate coherent structures from the rest of the flow^{10–16} and those that try to find the structures themselves by set oriented methods.^{9,17–22}

We recently developed a Lagrangian diagnostic that we term the finite-time curvature (FTC)²³ and that was designed

^{a)}Deceased.

^{b)}Electronic mail: bolltem@clarkson.edu

to study shape-coherent sets (that is, those that retain their shape as they are advected).²⁴ Here, we study the FTC field in more detail and show that it contains significant further information beyond shape coherence that can be used to quantify mixing. We compare the FTC to the more commonly known finite-time Lyapunov exponents (FTLEs) often used to identify Lagrangian coherent structures (LCSs) and show that the two contain similar and complementary, though not identical, information: FTLE can be thought of as the local propensity for stretching in a dynamical system, while FTC (appropriately extended to account for finite scale) additionally captures the local propensity for *folding*. Although stretching and folding often take place nearby each other in similar places, their spatial distribution is not identical;⁶ folding, as a nonlinear process, often occurs in areas where stretching is large, although the converse is not true. But since it is axiomatic that both stretching and folding are necessary for chaos,^{19,25–27} both kinds of information are needed to characterize chaotic mixing fully, and it is natural to ask about folding as well as stretching. Thus, the finite-scale FTC we introduce here usefully extends the toolbox that can be used to study mixing in complex flows from the Lagrangian standpoint. We note that a clear mathematical definition of folding is lacking in this context. Here, we argue that since the FTC defined in Eq. (3.1) describes the propensity for a material curve to develop curvature as time evolves, it is a sensible indicator of what is meant by folding in general terms. In dynamical systems, “folding” is often associated with the Smale horseshoe,²⁸ which may be taken as a complete fold of a region doubly across itself when a full shift symbolic dynamics results,^{29,30} and “less folding” or double covering results in a subshift.^{19,29,31} In the context of fluid dynamics, Theodorsen’s horseshoe vortex paradigm follows from constructing a model of individual hairpins.^{32–36} Even a bending in two directions, such as an inflection point, can eventually lead to horseshoes, as depicted in Fig. 1 of Ref. 37.

We begin below by reviewing the FTLE in Section II. In Section III, we review the definition of the FTC and generalize our previous methods to account for the effects of finite scale and resolution. We then illustrate our methods using experimental data from a quasi-two-dimensional laboratory flow in Section IV. Finally, we summarize our results in Section V.

II. REVIEW OF FINITE TIME LYAPUNOV EXPONENTS

The FTLE is a measure of local stretching in the flow. FTLEs are commonly used as indicators for hyperbolic LCSs,³⁸ since in hyperbolic regions of the flow, stretching is locally maximal. Even though FTLEs have shortcomings for the detection of LCSs (primarily that they also detect regions of high shear¹⁶), they remain perhaps the mostly widely used tool for studying Lagrangian coherence, particularly in experiments where more detailed information may not be available. Here, we briefly review the definition and properties of FTLEs, so that we may later compare and contrast them with FTC.

Given a velocity field $\mathbf{u}(\mathbf{x}, t)$ on a manifold $M \subset \mathbb{R}^d$, the trajectories $\mathbf{x}(t)$ of fluid elements are solutions of

$$\frac{d\mathbf{x}}{dt} = \mathbf{u}(\mathbf{x}, t), \quad (2.1)$$

where $\mathbf{x} \in M$ and $\mathbf{u}(\mathbf{x}, t)$ is at least $C^2(M)$. Integrating this equation yields the flow map $\phi_t^{t+\tau} : \mathbf{x}(t) \mapsto \mathbf{x}(t+\tau)$. The finite-time Cauchy–Green strain tensor of the velocity field along the trajectory $\mathbf{x}(t)$ is given by the symmetric, time-dependent, $d \times d$ matrix

$$J_\tau = \left[\frac{d\phi_t^{t+\tau} \mathbf{x}(t)}{d\mathbf{x}} \right]^* \frac{d\phi_t^{t+\tau} \mathbf{x}(t)}{d\mathbf{x}}, \quad (2.2)$$

where A^* denotes the adjoint of A . In the following, we assume that $d=2$, but this assumption is not mathematically necessary.

If over a finite time interval $[t, t+\tau]$ the minimum and maximum eigenvalues $\lambda_{\min}(\tau)$ and $\lambda_{\max}(\tau)$ of J_τ satisfy the condition

$$\ln \lambda_{\min}(\tau) < 0 < \ln \lambda_{\max}(\tau), \quad (2.3)$$

then the canonical local material advective behavior is described by the evolution of circles into ellipses, where the major axis of the ellipse lies along the direction of instability. This condition implies that there is compression in one direction and expansion in the other along the trajectory. Such a trajectory in a time-dependent velocity field is referred to as a *hyperbolic trajectory*.

Recall that the spectral norm of the Jacobian $\frac{d\phi_t^{t+\tau} \mathbf{x}(t)}{d\mathbf{x}}$ is given by

$$\left\| \frac{d\phi_t^{t+\tau} \mathbf{x}(t)}{d\mathbf{x}} \right\|^2 = \lambda_{\max}(\tau) \phi_t^{t+\tau}. \quad (2.4)$$

Then, the FTLE, which represents the maximum stretching at the point $\mathbf{x}(t)$ along the trajectory over a time τ , is given by

$$\sigma_\tau(\mathbf{x}(t)) = \frac{1}{|\tau|} \ln \left\| \frac{d\phi_t^{t+\tau} \mathbf{x}(t)}{d\mathbf{x}} \right\| = \frac{1}{|\tau|} \ln \sqrt{\lambda_{\max}(\tau)}. \quad (2.5)$$

It is common to define the repelling and attracting LCSs to be the ridges of the FTLE that are local maxima in space when computed in forward time ($\tau > 0$) and backward time ($\tau < 0$), respectively.^{39,40} Stated in terms relevant to our discussion here, the intensity of the FTLE field in a flow describes the propensity of ensembles of fluid elements that are nearby at time t to separate as the flow evolves.

Recall that, generally, a linear transformation of a circle yields an ellipse^{27,41} (see Fig. 1). Then, the positive semi-definite matrix J_τ in Eq. (2.5), as the strain formed from the variation of the flow $\frac{d\phi_t \mathbf{x}(t)}{d\mathbf{x}}$ along the orbit $\mathbf{x}(t)$, can be shown⁴¹ to have eigenvectors pointing along the major axis of the ellipse, and correspondingly the singular values are the lengths of the major axis corresponding to the growth rate of errors. We will derive further interpretation of this stretching picture of infinitesimal action along orbits below,

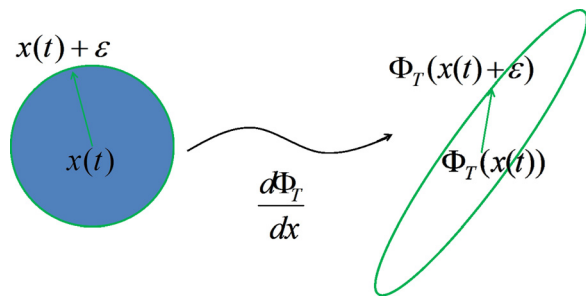


FIG. 1. On the finest scale, a small material circle of radius ε along the orbit of a point $\mathbf{x}(t)$ evolves to an ellipse, and this estimate describes that the linearity dominates. However, the geometry of the intermediate scale where this estimate differs from observation is described in Fig. 4, and the suggestion of Fig. 5 is that this transition between fine and intermediate scale may occur at smaller length scales than suggested by the common practice of studying only the linear terms.

as related to infinitesimal folding. Note that the finite-size Lyapunov exponent (FSLE)^{42,43} is conceptually similar to the FTLE but is computed slightly differently by measuring the time it takes for nearby particles to separate by some fixed amount. This computation is popular experimentally, especially in oceanography, since one can use discrete tracers such as buoys rather than densely seeding the system with particles on a fixed grid. However, it has been shown that, although related, the FSLE can be somewhat different from FTLE, particularly depending on details such as the numerical implementation and the particle seeding.⁴⁴

III. REVIEW AND COMPUTATION OF FINITE TIME CURVATURE

In our recent work,²³ we developed a direct Lagrangian measure of “curvature propensity,” which we termed the maximum finite-time curvature (maxFTC, or simply FTC), and which we used to infer the location of shape-coherent sets.²⁴ Here, we show that there is further structure to be found in the same computed field.

The idea of a shape-coherent set is that the general concept of “coherence” can be interpreted independently of the more commonly discussed direct notions of transport. That is, a set that maintains its shape to a high degree along its orbit can in a visceral way be considered to be coherent (specifically shape-coherent, in our terminology). We defined a measurement of this concept as $\sup_{S(A)} \frac{m(S(A) \cap \phi_T(A))}{m(B)}$,²⁴ where S is the set of all rigid body motions (that is, translations and rotations). Thus, for a given set A , we measured how closely a simple translation and rotation of A could be best matched to the true nonlinear flow $\phi_t^{t+\tau}$ of A . When the measured relative overlap can be made significantly close to unity, the set A is called “shape coherent.” With this notion in hand, simple geometric reasoning allows one to observe that the way to maintain shape is to maintain the curvature of the boundary of the set. Thus, investigating regions of space that have a very low propensity to change curvature may reveal such sets. This idea is closely related to the classical concept of curve congruence by matching curvature.⁴⁵ Thus, a shape-coherent set defined in this way is meant to correspond to a

set that mostly holds together under the flow. In Fig. 2, we have illustrated such a set (labeled (a), in the figure) in contrast to two other sets that have changed their shape. In Ref. 24, we recalled a tenet of differential geometry: the fundamental theorem of curvature indicates that the boundary curve can remain the same in time if and only if the curvature does not change. We showed that this idea can be made into a regularity theory that small changes in curvature correspond to small changes in shape coherence, and, conversely, that large changes in curvature are required to cause a set A to lose its shape coherence significantly. Note that other recent works studying other concepts of coherence have included figures comparable to Fig. 2, but with different back stories; in Fig. 1 of Ref. 46, two advected curves are described as remaining “coherent if an initially uniform material belt around it shows no leading-order variations in stretching after advection,” whereas relaxing a bit in Fig. 1 in Ref. 47 sets is described as coherent if they have boundaries that are small relative to their volume and that stay small. Both of these are stronger requirements as shape coherence allows arbitrary shapes as long as they have slowly changing boundary curvature.

We therefore defined the maxFTC $K_{t_0}^{t_0+\tau}(\mathbf{z})$ for a point \mathbf{z} in a plane $M \subset \mathbb{R}^2$ under a flow $\phi_{t_0}^{t_0+\tau}$ over the time interval $[t_0, t_0 + \tau]$ to be

$$K_{t_0}^{t_0+\tau}(\mathbf{z}) = \lim_{\varepsilon \rightarrow 0} \sup_{\|\mathbf{v}\|=1} \kappa(\phi_{t_0}^{t_0+\tau}(l_{\varepsilon, \mathbf{v}}(\mathbf{z}))), \quad (3.1)$$

where

$$l_{\varepsilon, \mathbf{v}}(\mathbf{z}) := \{\hat{\mathbf{z}} = \mathbf{z} + \varepsilon s \mathbf{v}, |s| < 1\}. \quad (3.2)$$

Here, \mathbf{v} is a unit vector and κ is the curvature. See Eq. (A2). So, $l_{\varepsilon, \mathbf{v}}(\mathbf{z})$ is a small line segment passing through the point $\mathbf{z} = (x, y)$, when $\varepsilon \ll 1$ (although note that the limit as $\varepsilon \rightarrow 0$ and the computation of curvature cannot in general be interchanged). The set of points $\phi_{t_0}^{t_0+\tau}(l_{\varepsilon, \mathbf{v}}(\mathbf{z}))$ yields a set of

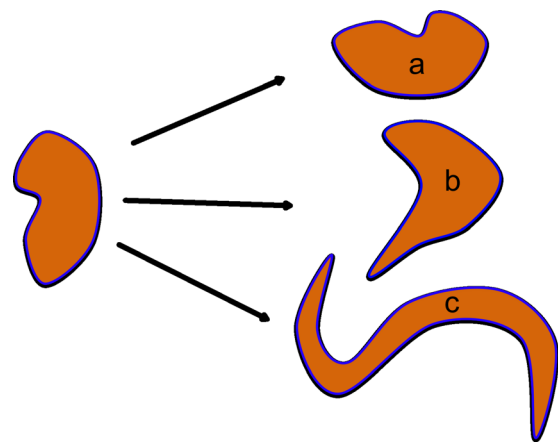


FIG. 2. A schematic of shape coherence. The idea of shape coherence for a given set (left) is that it should evolve under the nonlinear flow $\phi_t^{t+\tau}$ in a manner that is nearly a rigid body motion, namely, one composed of translation and rotation. Case (a) is such a scenario, whereas cases (b) and (c) both develop significant stretching and folding. In these later two cases, the curvature of the boundaries has changed from the original, most significantly at the points near where the arrows point.

curvatures $\kappa(\phi_{t_0}^{t_0+\tau}(l_{\varepsilon,\mathbf{v}}(\mathbf{z})))$ that is part of the supremum in Eq. (3.1). Interpretations of different estimates of this set are detailed below.

In practice, it is a computational challenge as to how we implement both the optimization step and the limit step ($\varepsilon \rightarrow 0$) in Eq. (3.1). As we discuss further below, on the finest spatial scales, there is a strong correlation between FTC and FTLE; on intermediate scales, however, they differ, as the FTC can uncover the nonlinearities in the flow. To distinguish these “finest” scales and “intermediate” scales precisely, we choose an $\varepsilon > 0$ and define a Finite-Scale Finite-Time Curvature (fsFTC) as

$$K_{t_0}^{t_0+\tau}(\mathbf{z}, \varepsilon) = \sup_{\|\mathbf{v}\|=1} \kappa(\phi_{t_0}^{t_0+\tau}(l_{\varepsilon,\mathbf{v}}(\mathbf{z}))). \quad (3.3)$$

In contrast to the FTC in Eq. (3.1), notice that the limit is omitted, and the argument explicitly includes the independent variable $\varepsilon > 0$. Equations (3.1) and (3.3) both contain the expression $\kappa(\phi_{t_0}^{t_0+\tau}(l_{\varepsilon,\mathbf{v}}(\mathbf{z})))$, which corresponds to a curvature computation on each of the set of points on the line segment(s) $l_{\varepsilon,\mathbf{v}}(\mathbf{z})$. That is, $\kappa(\phi_{t_0}^{t_0+\tau}(l_{\varepsilon,\mathbf{v}}(\mathbf{z}))) := \{\kappa\mathbf{w} : \mathbf{w} \in l_{\varepsilon,\mathbf{v}}(\mathbf{z})\}$ is a set of curvature values on which the sup is posed, across all line segments $l_{\varepsilon,\mathbf{v}}(\mathbf{z})$ in all orientations \mathbf{v} . Since the limit in Eq. (3.1) is taken after the curvature computation, this effectively selects the curvature at \mathbf{z} in the orientation in which it is maximal. We have written it in this manner with the limit so as to reflect the computational method for calculating the fsFTC described below in terms of estimates by small line segments. We emphasize here that we are most interested in small but not infinitesimal line segments; however, the full definition of the FTC in Eq. (3.1) is equivalent to measuring the maximal curvature of all advected line segments through the base point \mathbf{z} at $\phi_{t_0}^{t_0+\tau}(\mathbf{z})$. Furthermore and generally, for smooth flows, the sup should be realized and so can be replaced by a max operation. Note that the image of the line segment $l_{\varepsilon,\mathbf{v}}(\mathbf{z})$ is generally a curve $\phi_{t_0}^{t_0+\tau}(l_{\varepsilon,\mathbf{v}}(\mathbf{z}))$, and the role of the limit is to isolate the curvature to the locality of the image of the center point, at $\phi_{t_0}^{t_0+\tau}(\mathbf{z})$. In practice, the finite scale implicit in where and how the curvature is estimated in the neighborhood of $\phi_{t_0}^{t_0+\tau}(\mathbf{z})$ makes a difference for what is observed.

A. FTC on intermediate scales

The most straightforward interpretation of the estimation of the FTC by the fsFTC formula in Eq. (3.3) is by what we may refer to as the brute-force computation. First, choose n sample vectors \mathbf{v} pointed around a unit circle and uniformly spaced and scale these by a small but finite distance $\varepsilon > 0$ to form $\varepsilon\mathbf{v}$. The direction of each unit vector \mathbf{v} is specified by an angle γ . Then, form n triplets of points

$$A = \mathbf{z} - \varepsilon\mathbf{v}, \quad B = \mathbf{z}, \quad C = \mathbf{z} + \varepsilon\mathbf{v}, \quad (3.4)$$

approximating the line-segment instance of Eq. (3.2). Each can then be mapped forward under the flow to new locations

$$A' = \phi_{t_0}^{t_0+\tau}(\mathbf{z} - \varepsilon\mathbf{v}), \quad B' = \phi_{t_0}^{t_0+\tau}(\mathbf{z}), \quad C' = \phi_{t_0}^{t_0+\tau}(\mathbf{z} + \varepsilon\mathbf{v}) \quad (3.5)$$

after a finite time τ ; see Fig. 4 for an illustration. It is a fact of geometry that there is a unique circle passing through any three (non-colinear) points A', B', C' called the Menger circle. Calling the radius of this circle $R_{A',B',C'}$, the Menger curvature^{48–50} is defined as $\kappa_M(A', B', C') = 1/R_{A',B',C'}$. The Menger curvature may be computed by the convenient classical formula,

$$\kappa_M(A', B', C') = \frac{c}{2 \sin \gamma}. \quad (3.6)$$

See Fig. 3. Here γ may be chosen as any one of the 3 angles of the triangle $A'B'C'$ described by the three points and c is the length of the corresponding opposite side. Note that order of labeling is not important, as the circle is uniquely defined by the three points.

The unit vectors $\mathbf{v} = (\cos(s), \sin(s))$ for each $s \in [0, 2\pi)$ specify points (A, B, C) and their images (A', B', C') in Eqs. (3.4) and (3.5) for each angle. We may then write $\kappa_M(s, \varepsilon) := \kappa_M(A', B', C')$. Referring to Fig. 4 for labeling, each of the n uniformly sampled points around a circle of radius ε , $s_i = ih$, $h = 2\pi/n$, $i = 0, 1, \dots, (n-1)$, yields a sample of the function by points $(s_i, \kappa_M(s_i, \varepsilon))$. See Fig. 4. From this finite sample we may estimate

$$K_{t_0}^{t_0+\tau}(\mathbf{z}, \varepsilon) \approx \max_i \{\kappa_M(s_i, \varepsilon)\}, \quad (3.7)$$

for fixed ε .

Proceeding more carefully, but still on a finite intermediate scale with $\varepsilon > 0$, we can estimate the fsFTC, which then will give us an estimate of the FTC. Unlike the above procedure, where we simply selected the maximal value from a large sampling, a more efficient and accurate way to optimize any function is to use a standardized optimization algorithm such as the gradient descent method.⁵¹ This approach will work if the flow $\phi_{t_0}^{t_0+\tau}$ is sufficiently smooth at \mathbf{z} . It then follows that the fsFTC $K_{t_0}^{t_0+\tau}(\mathbf{z}, \varepsilon)$ can be estimated by the optimal Menger curvature \mathbf{z} for a given small ε , so that

$$K_{t_0}^{t_0+\tau}(\mathbf{z}, \varepsilon) \approx \max_{s \in [0, 2\pi)} \{\kappa_M(s, \varepsilon)\}, \quad (3.8)$$

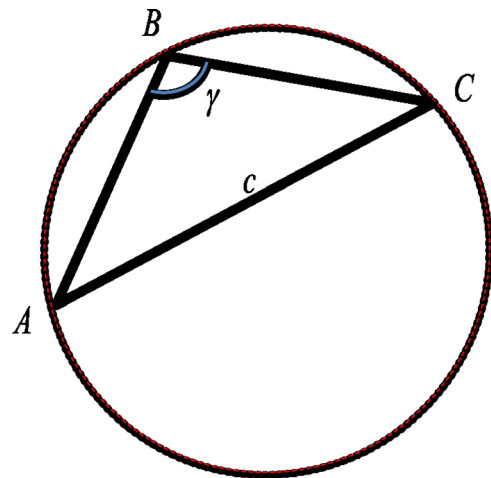


FIG. 3. Menger curvature of three points A, B, C is defined in terms of the radius of the unique circle passing through these points by formulas, Eqs. (3.4) and (3.6).

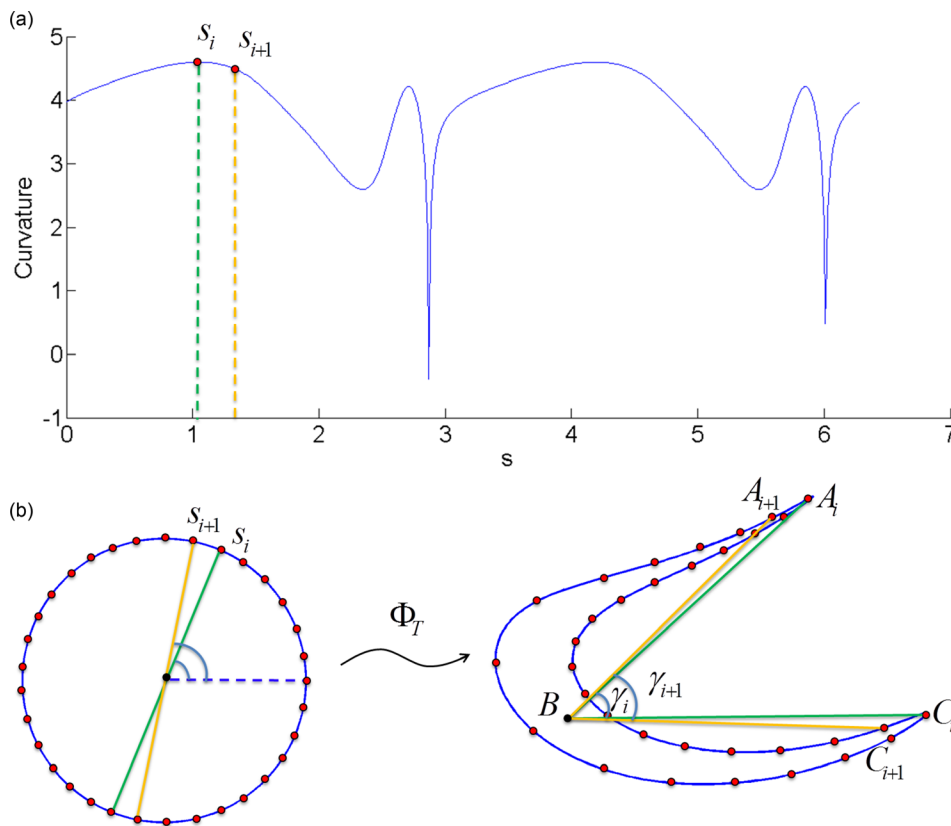


FIG. 4. Curvature due to sampling 3 opposing points along a line segment $l_{\epsilon, \mathbf{v}}$ for $n = 33$ line segments with angular positions s_i uniformly around a small circle, according to Eqs. (3.4)–(3.5), and estimating curvature of the image by the Menger curvature by Eq. (3.6). See also Fig. 5. The intermediate scale gives rise to (a) curvature as a function of s , angle in radians around the circle, that differs significantly from the fine scale seen by the limit curve in Fig. 5, related to the prediction Eq. (A2). (b) In this intermediate scale, the image of a circle is not simply an ellipse as suggested by Fig. 2, but rather there may be significant folding nonlinearities as shown here. In the regions of phase space where folding is prominent, this effect can be significant.

where we already noted that the image of the line segment $l_{\epsilon, \mathbf{v}}(\mathbf{z})$ is the curve $\phi_{t_0}^{t_0+\tau}(l_{\epsilon, \mathbf{v}}(\mathbf{z}))$; the Menger curvature $\kappa_M(A', B', C')$ is used here as an estimator of the curvatures in the neighborhood of $\phi_{t_0}^{t_0+\tau}(l_{\epsilon, \mathbf{v}}(\mathbf{z}))$, assuming small ϵ and smooth $\phi_{t_0}^{t_0+\tau}$. See Fig. 4. The function $\kappa_M(s, \epsilon)$ shown in Fig. 4(a) shows complex structure that is due to the finite, non-zero $\epsilon > 0$. In contrast, as shown below, for the finest scales where $\epsilon \ll 1$, $\kappa_M(s, \epsilon)$ displays only simple periodic behavior of the ellipse with respect to s . We emphasize that this observation is not simply an issue with estimation for nonzero ϵ ; as we demonstrate below, the transition between intermediate and fine scales may occur at extremely small ϵ compared with observable scales in experiments. More interestingly, however, we also show that we can use the inherent finite-scale nature of the fsFTC to infer information about the flow nonlinearities.

Finally in this section, we make a remark for clarity and contrast. There are different kinds of circles that are drawn here, with different meanings. Fig. 3 describes a general circle, relating to the inverse of the radius of an osculating circle (originally named the “circulus osculans,” or kissing circle, by Leibniz) that touches the curve at a single point,^{52,53} which is one classical way to begin the discussion of curvature (alternatively to beginning the discussion with the rate of change of the tangent vector with respect to arc length). In Fig. 3, we show how the Menger curvature^{48,49} is an estimator of curvature, particularly if A and C are close to B . Separately, the concept of FTC and fsFTC at a point \mathbf{z} is described in terms of line segment through a point \mathbf{z} such that when a material curve flows forward in time, this segment develops maximal curvature. Since the set of all such

line segments of radius ϵ describes a disc, we draw the images of discs in Fig. 4. Since the curvature is taken before the limit in Eq. (3.1), we are indeed defining the curvature of the image of a material line, and to estimate this, we use an intermediate scaled triplet of points and the Menger formula. The circle in Fig. 4 is the most salient for our purposes here; the rest are drawn for geometric discussion and computation. Finally, there is an estimate of the curvature in the Appendix in terms of a small line segment through a point that may be at the edge of a circle centered on a nearby point, and from this, we get an estimate on the fine scales.

B. FTC on the finest scales

For fine scales with $\epsilon \ll 1$, small enough that the image of a circle of radius ϵ about \mathbf{z} is essentially an ellipse with minimal non-affine distortion, the computation of FTC simplifies to an analytic expression that we describe here. In this case, the smallness of the scale effectively linearizes the action of the flow, meaning that the FTC can no longer capture the propensity of the flow to fold curves. In fact, under the action of a linear flow, the image of a line is exactly a line. Hence, one may deduce that following small line segments by the above definitions would suggest there is zero propensity for the flow to develop curvature. However, by the discussion in the Appendix, and referring to Fig. 7, we show that under finite precision computation, where three points on a straight line are represented by three points that are not quite collinear, then some curvature is nonetheless measured. However, the curvature measured is in fact related to the linear flow of $D = \frac{d\phi_t^{t+\tau}(\mathbf{x}(t))}{d\mathbf{x}}$.

Write correspondingly the strain as $J_\tau = D^*D$. We can apply a singular value decomposition (SVD) to D , obtaining $D = U\Sigma V^*$. $\Sigma = \text{diag}(\sigma_1, \sigma_2)$ is the diagonal matrix whose nonzero entries are the major and minor axis lengths of the image ellipse of the unit circle shown; equivalently, they are eigenvalues of J_τ . $V = [v_1|v_2]$ is the orthogonal matrix whose orthogonal column vectors are oriented along the major and minor axes of the image ellipse and are also the right eigenvectors of J_τ , which, without loss of generality, we have illustrated for convenience to be oriented along the x and y axes and we take $\mathbf{z} = 0$. We have included a point $\mathbf{w} = (\sigma_1, 0)$, without loss of generality at angle $s=0$, along the major axis v_1 . $\bar{\mathbf{w}} = (r\sigma_1, 0)$ is the corresponding point on the concentric ellipse shown. We also illustrate in Fig. 7 a red line segment of length 2δ that gives the Menger image with sides $\bar{\delta}$ through \mathbf{w} .

Let us now consider the development of curvature by the local dynamics as suggested by Fig. 7. The Menger curvature through the points on the ellipse shown in Fig. 7, $A' = (\sigma_1 r \cos(s), \sigma_2 r \sin(s))$, $B' = \bar{\mathbf{w}} = (r\sigma_1, 0)$, and $C' = (\sigma_1 r \cos(s), -\sigma_2 r \sin(s))$, estimates the curvature of the ellipse at $\bar{\mathbf{w}}$. Specifically,

$$\lim_{s \rightarrow 0} \kappa_M(A', \bar{\mathbf{w}}, C') = \kappa(\bar{\mathbf{w}}) = \frac{\sigma_1}{r\sigma_2^2}. \quad (3.9)$$

The first part of this equality follows from the continuity property of Menger curvature: for smooth curves, if the three points $A', \bar{\mathbf{w}}, C' \rightarrow \bar{\mathbf{w}}$, then the Menger curvature limits to the curvature at the point. The computation of the second part of the equality is detailed in the Appendix. In stating the next limit, notice that Eq. (3.10) differs from Eq. (3.9) in that $\bar{\mathbf{w}}$ and \mathbf{w} are similarly positioned, but on concentric ellipses. Considering concentric circles of radius $r > 1$, the Menger curvature of the points shown in Fig. 7, $A' = (\sigma_1 r \cos(s), \sigma_2 r \sin(s))$, $B' = \mathbf{w} = (\sigma_1, 0)$, and $C' = (\sigma_1 r \cos(s), -\sigma_2 r \sin(s))$, are estimated by the curvature of the ellipse at $\bar{\mathbf{w}}$, since $\bar{\mathbf{w}} \rightarrow \mathbf{w}$ as $r \rightarrow 1$, so that

$$\lim_{\mathbf{w} \rightarrow \mathbf{w}} \kappa_M(A', \mathbf{w}, C') = \kappa(\mathbf{w}) = \frac{\sigma_1}{\sigma_2^2}. \quad (3.10)$$

It then follows that if the flow $\phi_{t_0}^{t_0+\tau}$ at \mathbf{z} is continuously differentiable, the FTC is estimated by the limit of curvatures as

$$\begin{aligned} K_{t_0}^{t_0+\tau}(\mathbf{z}) &= \lim_{\varepsilon \rightarrow 0} K_{t_0}^{t_0+\tau}(\mathbf{z}, \varepsilon) \sim \max_{s \in [0, 2\pi]} \{ \kappa_M(s, \varepsilon) \} \\ &\sim \max \left\{ \frac{\sigma_1}{\sigma_2^2}, \frac{\sigma_2}{\sigma_1^2} \right\}, \end{aligned} \quad (3.11)$$

where the terms are, in order, the FTC, the fsFTC, the maximum Menger curvature evolved from center of the circle according to Eq. (3.8), and the maximum ratio of the singular values. If furthermore the flow is area-preserving, then $\sigma_1 = 1/\sigma_2$. Hence, in this special case, $\frac{\sigma_1}{\sigma_2^2} = \sigma_1^3$, $\frac{\sigma_2}{\sigma_1^2} = \sigma_2^3$, and so $K_{t_0}^{t_0+\tau}(\mathbf{z}) = \sigma_1^3$. The arguments supporting these statements in the Appendix are straightforward. We note that one can construct some special cases where the estimate in Eq. (3.11) does not perform well; however, such cases are not generic.

In Section III C, we interpret consequences both for the relationship of the study of curvature evolution to coherence, hyperbolicity, and the contrast of scales. Below, we will discuss then how it is often the intermediate-scale folding that presents the interesting features.

C. Contrast of scales

As noted above, the FTC should be interpreted in different ways depending on the spatial scale on which it is applied. Specifically, consider Fig. 5, where we plot profiles of the curvatures around the circle for decreasing $\varepsilon = 10^{-1}, 10^{-2}, \dots, 10^{-7}$. We indicate the transition that separates the intermediate scale from the fine scale at roughly $\varepsilon = 10^{-2}$, where the local circle of line segments exhibits significant folding, from the finest scales, where it shows the simpler curvature of ellipses behavior predicted by Eqs. (3.9)–(3.11),

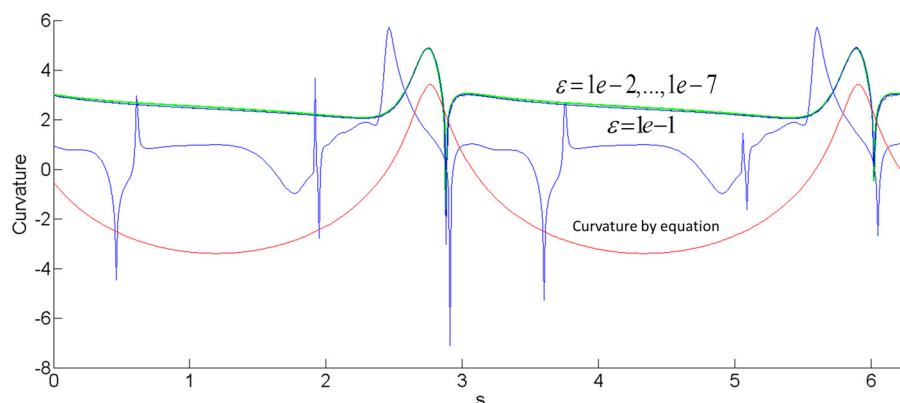


FIG. 5. Curvature as a function of angle $0 \leq s < 2\pi$ around the circle, with ε decreasing in decades. Compare this picture to Fig. 4, where we show how the details of the fsFTC (Eq. (3.3)) involve estimates of the way in which small line segments $l_{e,v}$ (Eq. (3.2)) through the center point \mathbf{z} each yield an estimated curvature by the Menger formula (Eq. (3.6)) in Eq. (3.7). Considering each line segment through the center point yields a curve of curvature values, one for each possible angle s specifying the rotational orientation of the initial line segment $l_{e,v}$. Here, $\varepsilon \approx 10^{-2}$ roughly corresponds to the transition between the intermediate and finest scales. The system used is the standard, non-autonomous double gyre, given by $\dot{x} = -\pi A \sin(\pi f(x, t)) \cos(\pi y)$, $\dot{y} = \pi A \cos(\pi f(x, t)) \sin(\pi y) \frac{df}{dx}$, $f(x, t) = \varepsilon \sin(\omega t) x^2 + (1 - 2\varepsilon \sin(\omega t))x$ with parameters $A = 0.1$, $\varepsilon = 0.1$, and $\omega = 2\pi/10$. The gyre was run for a time of $T = 20$, and the curves here correspond to an initial condition of $(0.1240, 0.1200)$. Note that we see convergence of the curvature estimates—the blue curves accumulating on the green—and that for maximal values, the red curve as described by values around a circle occur at maximal position suggested by the discussion in the Appendix.

(A2). Figure 5 illustrates the two somewhat different types of information contained in the FTC. To restate these two aspects more descriptively, *minimal* values of the FTC mark regions in the flow where material curves change spatiotemporally slowly. This feature of the FTC was the original reason we developed the analysis,²³ as it can be used to locate shape-coherent sets.²⁴ The converse, however, also holds: *maximal* values of the FTC indicate regions where material curves most rapidly develop curvature, and thus the places in the flow where the shape of a set changes most rapidly.

How can we understand these opposite aspects in more familiar terms? The description in terms of shape coherence suggests that it is the elliptic-like behavior of the flow that causes the low troughs of the FTC field. Hyperbolic material curves, however, will cause any transverse curve of material to deform rapidly, suggesting that *ridges* of the FTC field likely indicate hyperbolic behavior. Thus, the single FTC computation can be used to locate both hyperbolic (ridges) and elliptic (valleys) regions of the flow field.

The analysis above in Eqs. (3.9)–(3.11) affirms that there is a strong relationship between FTC and FTLE on fine scales, since both are related to the singular values of the Jacobian matrices along the flow. But, on the finest spatial scale, Eq. (3.11) shows that FTC is related to the *cube* of the FTLE. This feature has an important consequence: one would expect that ridges of the FTC field will be more prominent and will appear for shorter advection times than ridges of the FTLE field. We expect, heuristically even if not in detail, that this feature will be retained even on coarser scales since the general notion that hyperbolicity emphasizes deformation of material curves is generally understood by consideration of a transverse curve that samples the flow and becomes exponentially deformed. The more rapid appearance of structure in the FTC field makes it a promising candidate for forecasting applications, since less future-time information is needed to locate hyperbolic regions. Both complimentary aspects of coherence are revealed in a FTC field.

IV. EXPERIMENTAL DEMONSTRATION

To illustrate the similarities and differences between the FTC and the FTLE in a practical example and to demonstrate that they are computable using real data, we measured both using experimental data from a quasi-two-dimensional laboratory flow. The details of this experiment have been described previously.^{54–56} Briefly, we used a thin electromagnetically driven layer of an electrolytic fluid to produce nearly two-dimensional flow. The working fluid was a layer of salt water (16% NaCl by mass in deionized water) measuring $86 \times 86 \times 0.5 \text{ cm}^3$ that rested on a glass plate coated with a hydrophobic wax. A square array of permanent neodymium-iron-boron magnets with vertical dipole moments and a lateral spacing of $L_m = 2.54 \text{ cm}$ lies beneath the glass; here, the magnets were arranged in stripes of alternating polarity. By running an electric current (of 1.25 A for the experiments analyzed here) through the salt water, we generated a Lorentz body force on the fluid that set it into motion. The Reynolds number $\text{Re} = UL_m/\nu$, based on the in-plane

root-mean-square velocity U , the magnet spacing, and the kinematic viscosity ν , was 270.

We measured the velocity field using particle tracking velocimetry (PTV). The electrolyte was seeded with 50- μm -diameter fluorescent polystyrene microspheres; as the spheres are somewhat less dense than the electrolyte, they rise to its surface. To eliminate long-range surface-tension-driven forces between the floating particles, we floated a layer of pure water 5 mm deep on top of the electrolyte. We imaged the motion of the particles in the central $31.7 \times 23.6 \text{ cm}^2$ (roughly $12.5 \times 9 L_m$) of the apparatus using a 4 megapixel IDT MotionPro M5 camera at a rate of 60 frames per second. We then tracked about 30 000 particles per frame using a multi-frame predictive tracking algorithm⁵⁷ and computed time-resolved velocities from the trajectories by convolving them with a smoothing and differentiating kernel.⁵⁸ Finally, we used the instantaneous velocities of all the tracked particles to create velocity fields by projecting the data onto the eigenmodes of a streamfunction,⁵⁴ removing noise from the data and ensuring that the measured velocity fields are reliably two-dimensional.

In Fig. 6, we show both the FTC and the FTLE computed over the same time window for the experiment. Even though it is high, the experimental resolution is still finite; thus, the FTC plotted here should be interpreted as the fsFTC, and we may expect it to display finite-scale features—most importantly, the folding propensity of the flow.

The FTLE (Fig. 6(b)) contains the features that are typically seen in this kind of flow. Most of the field is filled with relatively small, though still positive, values, indicating that the full field mixes chaotically, but relatively weakly. The FTLE also reveals very strongly stretching regions that are nearly co-dimension one; these line-like regions should approximately correspond to the Lagrangian coherent structures in the flow. In the cores of the areas in between the FTLE ridges, the FTLE values go negative, marking regions that are elliptic in character.

Comparing the FTLE with the fsFTC shown in Figs. 6(a) and 6(b), it is clear that the fsFTC reveals some of the same features, even though the FTLE captures only stretching while the fsFTC additionally captures folding. This rough spatial correspondence between strong stretching and strong folding is not surprising and has been demonstrated before.⁶ Here, however, for the same integration time (which was fixed for both panels in Fig. 6), these features are sharper for the fsFTC: the colormap for the fsFTC in Fig. 6(b) is on a logarithmic scale, while it is on a linear scale for the FTLE in Fig. 6(a). This kind of rapid convergence is very useful in experimental or observational applications, where long records of future flow-field information may not be available. But more than this simple difference, the fsFTC reveals additional structure. Regions where the fsFTC is small are not simply not stretching; they are also, by construction, *not folding* and are thus evolving as semi-rigid bodies over the time window used to calculate the fsFTC. This kind of behavior should be contrasted with structures such as the Great Red Spot on Jupiter, where a macroscopic region of the flow is elliptic in that it is separated from the rest of the flow by a persistent transport barrier, but where the flow

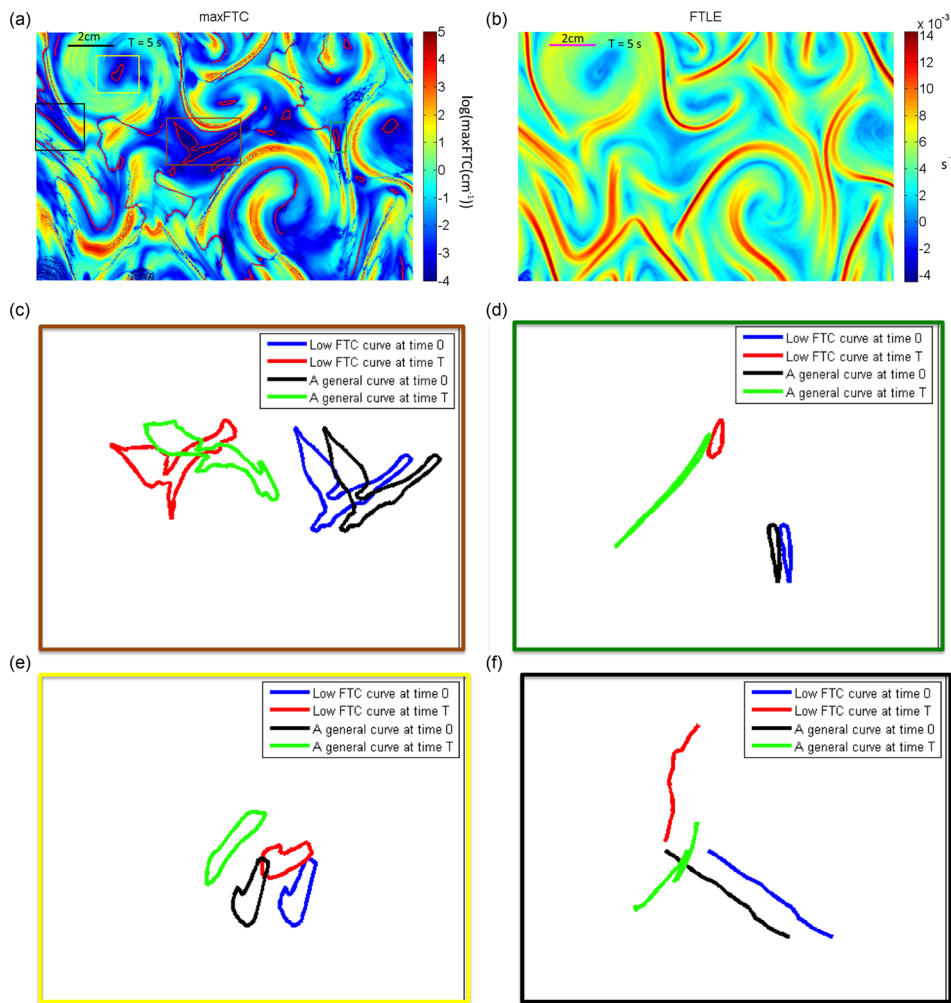


FIG. 6. A (a) FTC field and a (b) FTLE field computed for the same data from the quasi-two-dimensional laboratory flow. Integration time for both fields is $5s \approx 3T_L$, where $T_L = L_m/U$ is the eddy turnover time. Note that in the FTLE and FTC, many of the same features are seen in both methods of analysis (cohabitating of the high FTLE ridges and FTC ridges), but if we look closely, there are many places where the two are telling different stories. Separately, since the FTC was designed to reveal shape coherence in the troughs of the FTC, then this figure is highlighting several such regions—boxed and blown up. So as initial, and after evolution, (blue then red), those troughs clearly reveal that the shape is mostly the same. This is a sensitive property in that even very nearby same-shaped starting curves (black) become highly deformed after the same time epoch shown (green). (c)–(f) demonstrate that low FTC troughs maintain high shape coherence but not general curves.

inside the barrier is still highly turbulent. For macroscopic areas where the fsFTC is small throughout, we expect that the internal flow is not only distinguished from the external flow but is also evolving simply and not in a turbulent or chaotic fashion. Of additional note are the thin lines of low fsFTC values; these minimal curves of the fsFTC behave as they are nearly rigid, and so they can rotate as time evolves but cannot bend.

V. SUMMARY

Chaotic mixing can be described schematically as a repeated process of the stretching and folding of material volumes; both of these processes are required to produce efficient mixing in a volume-preserving flow. By explicitly considering the effects of finite resolution on the finite-time curvature, we have shown here that this fsFTC naturally contains information about both stretching and folding. Thus, we have demonstrated that the FTC can be used to indicate more than the shape coherence it was designed for. We illustrated the utility of the fsFTC by computing both it and the more common FTLE on experimental data from a laboratory flow, showing that the fsFTC is simply computable and that it tends to reveal sharp features more rapidly than the FTLE. Thus, the fsFTC we have introduced is a valuable addition to the growing collection of Lagrangian methods that can be

used to explore and characterize mixing and transport in complex flows.

ACKNOWLEDGMENTS

N.T.O. acknowledges support from the U.S. National Science Foundation under Grant Nos. DMR-1206399 and DMS-1211952. E.M.B. and T.M. were supported by the Office of Naval Research and E.M.B. was also supported by the Army Research Office, the National Geospatial Intelligence Agency, and the National Science Foundation under CMMI 1129859.

APPENDIX

Here, we prove the statement in Eqs. (3.9) and (3.10) regarding the ratio of singular values. It is well known that the image of a circle (that is, the set of all unit vectors) is an ellipse under the action of a general 2 by 2 matrix D . Curvature at a point is defined as the inverse of the radius of the osculating (tangent) circle to a curve at the point. Thus, a unit circle has curvature $\kappa = 1$ by definition. Now, we will show that the growth of curvature of the circle will be related to the ratio of singular values according to Eqs. (3.9) and (3.10) and also that the computed Menger curvature of “line segments” will give the same under the condition of (1) small line segments and (2) small enough that in general configuration that a small amount of numerical imprecision will creep into the estimate.

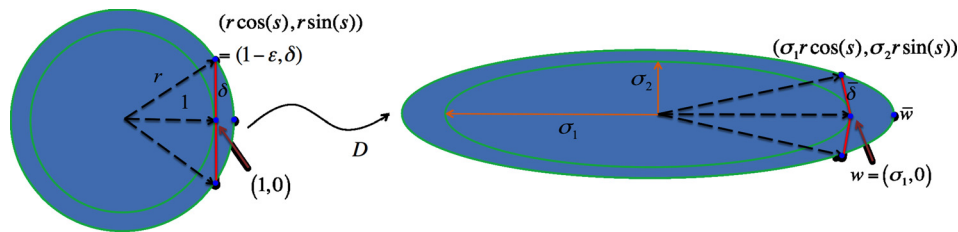


FIG. 7. Two concentric circles of radius 1 and $r > 1$, each parameterized by angle s , and correspondingly the right triangle shown with sides, 1, δ , and r . The center is shown as $(0, 0)$. In the Appendix, we follow the curvature growth of a “slightly perturbed” straight line (left shown in red) chosen perpendicular to the pre image of the dominant singular vector as shown, with coordinates $(1 - \epsilon, \delta)$, $(1, 0)$, and $(1 - \epsilon, -\delta)$ and the image under a linear transformation $D = \text{diag}(\sigma_1, \sigma_2)$.

This second part is both always present in real computations, and necessary for the result, since in exact arithmetic, the image of a line is a line under a linear transformation.

Let the image of the circles shown in Fig. 7 be the ellipses shown, where without loss of generality, the body axes are aligned with the coordinate axes for convenience as shown, and the major axes v_1 and v_2 have lengths σ_1 and σ_2 from the SVD $D = U\Sigma V^*$. The inner ellipse shown can be written implicitly as $\frac{x^2}{\sigma_1^2} + \frac{y^2}{\sigma_2^2} = 1$, or parametrically as

$$\gamma(s) = \langle \sigma_1 \cos s, \sigma_2 \sin s \rangle. \quad (\text{A1})$$

By a standard computation of the curvature in terms of a parametrically represented curve, it follows that

$$\kappa(s) = \frac{|\gamma'(s) \times \gamma''(s)|}{|\gamma'(s)|^3} = \frac{\sigma_1 \sigma_2}{|\sigma_1^2 \sin^2(s) + \sigma_2^2 \cos^2(s)|^{3/2}}. \quad (\text{A2})$$

Solving $\kappa'(\hat{s}) = 0$ for the critical points \hat{s} yields $\hat{s} = 0, \frac{\pi}{2}$, and hence the extrema of curvature are found by substitution into Eq. (A2) to be

$$\kappa(\hat{s}) = \left\{ \frac{\sigma_1}{\sigma_2^2}, \frac{\sigma_2}{\sigma_1^2} \right\}. \quad (\text{A3})$$

Likewise, the curvatures of the inner and outer ellipses at \mathbf{w} and $\bar{\mathbf{w}}$, respectively, are $\kappa(\mathbf{w}) = \frac{\sigma_1}{\sigma_2^2}$ and $\kappa(\bar{\mathbf{w}}) = \frac{\sigma_2}{\sigma_1^2}$. The limit in Eq. (3.9) follows immediately since the cosine and sine functions in the parametric equation of an ellipse (Eq. (A1)) are continuous.

Alternatively, now consider the computation of the growth ratio of Menger curvature of the slightly bent line segment shown in Fig. 7. Let us label the three points as $P_1 = (1, 0)$, $P_2 = (1 - \epsilon, \delta)$, and $P_3 = (1 - \epsilon, -\delta)$. For an exactly straight line, $\epsilon = 0$; however, due to finite precision arithmetic, we are considering $0 < \epsilon \ll 1$, and further, discussing a small line segment, we choose $\delta \ll 1$, but not nearly as small as the arithmetic precision so that $\epsilon \ll \delta$. First, we compute the Menger curvature of the (left) line segment shown by Eq. (3.6). Let us define the vectors

$$\begin{aligned} \mathbf{a} &= P_1 - P_2 = \langle P_1.x - P_2.x, P_1.y - P_2.y \rangle = \langle \epsilon, -\delta \rangle, \\ \mathbf{b} &= P_1 - P_3 = \langle P_1.x - P_3.x, P_1.y - P_3.y \rangle = \langle \epsilon, \delta \rangle, \\ \mathbf{c} &= P_2 - P_3 = \langle P_2.x - P_3.x, P_2.y - P_3.y \rangle = \langle 0, -2\delta \rangle. \end{aligned} \quad (\text{A4})$$

Note that for simplicity of presentation, we have chosen the same computational “error” in both the points P_2 and P_3 , rather than separate errors ϵ_1 and ϵ_2 . Our conclusions and

results do not change, however, if $\epsilon_1 \neq \epsilon_2 \neq \epsilon$, as can be readily checked. Now, let $\gamma = \angle P_2 P_1 P_3$. By the standard definition of the cross product, $|\sin(\gamma)| = \|\mathbf{a} \times \mathbf{b}\| / \|\mathbf{a}\| \|\mathbf{b}\|$ (interpreting \mathbf{a} and \mathbf{b} as three-dimensional vectors with zero in the third component, as usual), and

$$\begin{aligned} \|\mathbf{a} \times \mathbf{b}\| &= \|\mathbf{a}; \mathbf{b}\| = \begin{vmatrix} \epsilon & -\delta \\ \epsilon & \delta \end{vmatrix} = 2\epsilon\delta, \\ \|\mathbf{a}\|^2 &= \|\mathbf{b}\|^2 = \epsilon^2 + \delta^2, \end{aligned} \quad (\text{A5})$$

we have

$$\sin(\gamma) = \frac{2\epsilon\delta}{\epsilon^2 + \delta^2}. \quad (\text{A6})$$

Then, from the Menger formula (Eq. (3.6)) and substitution, we have

$$\begin{aligned} \kappa_M(P_2, P_1, P_3) &= \frac{\mathbf{c}}{2 \sin(\gamma)} = \frac{\|\mathbf{a}\| \|\mathbf{b}\| \|\mathbf{c}\|}{2 \|\mathbf{a}; \mathbf{b}\|} \\ &= \frac{(\epsilon^2 + \delta^2) 2\delta}{2\epsilon\delta} = \frac{\epsilon^2 + \delta^2}{2\epsilon}. \end{aligned} \quad (\text{A7})$$

Remembering our assumptions that $\epsilon \ll \delta \ll 1$, $\kappa_M(P_2, P_1, P_3) \sim 0$, consistent with a small (almost) straight line. Under the linear transformation $D = \text{diag}(\sigma_1, \sigma_2)$ shown in Fig. 7, the three the points in Eq. (A4) map to

$$\begin{aligned} \mathbf{a}' &= P'_1 - P'_2 = \langle P_1.x' - P_2.x', P_1.y' - P_2.y' \rangle = \langle \sigma_1\epsilon, -\sigma_2\delta \rangle, \\ \mathbf{b}' &= P'_1 - P'_3 = \langle P_1.x' - P_3.x', P_1.y' - P_3.y' \rangle = \langle \sigma_1\epsilon, \sigma_2\delta \rangle, \\ \mathbf{c}' &= P'_2 - P'_3 = \langle P_2.x' - P_3.x', P_2.y' - P_3.y' \rangle = \langle 0, -2\sigma_2\delta \rangle \end{aligned} \quad (\text{A8})$$

and the angle at the image is $\gamma' = \angle P'_2 P'_1 P'_3$. Correspondingly

$$\begin{aligned} \|\mathbf{a}' \times \mathbf{b}'\| &= \|\mathbf{a}'; \mathbf{b}'\| = \begin{vmatrix} \sigma_1\epsilon & -\sigma_2\delta \\ \sigma_1\epsilon & \sigma_2\delta \end{vmatrix} = 2\sigma_1\sigma_2\epsilon\delta, \\ \|\mathbf{a}'\|^2 &= \|\mathbf{b}'\|^2 = \sigma_1^2\epsilon^2 + \sigma_2^2\delta^2, \\ \sin(\gamma') &= \frac{2\sigma_1\sigma_2\epsilon\delta}{\sigma_1^2\epsilon^2 + \sigma_2^2\delta^2}, \end{aligned} \quad (\text{A9})$$

from which the Menger curvature of the image points becomes

$$\begin{aligned} \kappa_M(P'_2, P'_1, P'_3) &= \frac{\mathbf{c}'}{2 \sin(\gamma')} = \frac{\|\mathbf{a}'\| \|\mathbf{b}'\| \|\mathbf{c}'\|}{2 \|\mathbf{a}'; \mathbf{b}'\|} \\ &= \frac{(\sigma_1^2\epsilon^2 + \sigma_2^2\delta^2) 2\delta}{2\sigma_1\sigma_2\epsilon\delta} = \frac{\sigma_1^2\epsilon^2 + \sigma_2^2\delta^2}{2\sigma_1\epsilon}. \end{aligned} \quad (\text{A10})$$

Finally, we compute the ratio of the growth of the Menger curvature using Eqs. (A7) and (A10)

$$\frac{\kappa_M(P_2, P_1, P_3)}{\kappa_M(P'_2, P'_1, P'_3)} = \frac{\epsilon^2 + \delta^2}{2\epsilon} \bigg/ \frac{\sigma_1^2 \epsilon^2 + \sigma_2^2 \delta^2}{2\sigma_1 \epsilon} \sim \frac{\delta^2}{2\epsilon} \bigg/ \frac{\sigma_2^2 \delta^2}{2\sigma_1 \epsilon} = \frac{\sigma_1}{\sigma_2^2}. \quad (\text{A11})$$

This last estimate in Eq. (A11) again follows from the assumption $\epsilon \ll \delta \ll 1$, and hence we see that for small line segments, under finite precision, the limiting behavior of true curvatures of the circle evolving into the ellipse Eq. (A3) is related to ratios of singular values.

In the case that $\epsilon_1 \neq \epsilon_2$, it is straightforward to check, modifying the position of the points in Eqs. (A4)–(A8) slightly, that the resulting curvature of the almost collinear points and its image are

$$\begin{aligned} \kappa_M(P_2, P_1, P_3) &= \frac{\sqrt{(\epsilon_1^2 + \delta^2)(\epsilon_2^2 + \delta^2)((\epsilon_1 - \epsilon_2)^2 + \delta^2)}}{2(\epsilon_1 + \epsilon_2)\delta} \\ \kappa_M(P'_2, P'_1, P'_3) &= \frac{\sqrt{(\sigma_1^2 \epsilon_1^2 + \sigma_2^2 \delta^2)(\sigma_1^2 \epsilon_2^2 + \sigma_2^2 \delta^2)((\sigma_1 \epsilon_1 - \sigma_1 \epsilon_2)^2 + \sigma_2^2 \delta^2)}}{2\sigma_1 \sigma_2 (\epsilon_1 + \epsilon_2)\delta} \end{aligned} \quad (\text{A12})$$

and that therefore the above computation, based on assuming $\epsilon = \epsilon_1 = \epsilon_2$, does not change the asymptotic result Eq. (A11).

- ¹O. Reynolds, "Study of fluid motion by means of coloured bands," *Nature* **50**, 161–164 (1894).
- ²H. Aref, "Stirring by chaotic advection," *J. Fluid Mech.* **143**, 1–21 (1984).
- ³B. I. Shraiman and E. D. Siggia, "Scalar turbulence," *Nature* **405**, 639–646 (2000).
- ⁴B. Sawford, "Turbulent relative dispersion," *Annu. Rev. Fluid Mech.* **33**, 289–317 (2001).
- ⁵E. Shuckburgh and P. Haynes, "Diagnosing transport and mixing using a tracer-based coordinate system," *Phys. Fluids* **15**, 3342–3357 (2003).
- ⁶D. H. Kelley and N. T. Ouellette, "Separating stretching from folding in fluid mixing," *Nat. Phys.* **7**, 477–480 (2011).
- ⁷N. T. Ouellette, "On the dynamical role of coherent structures in turbulence," *C. R. Phys.* **13**, 866–877 (2012).
- ⁸I. Mezić, S. Loire, V. A. Fonoberov, and P. Hogan, "A new mixing diagnostic and gulf oil spill movement," *Science* **330**, 486–489 (2010).
- ⁹E. M. Boltt, A. Luttmann, S. Kramer, and R. Basnayake, "Measurable dynamics analysis of transport in the Gulf of Mexico during the oil spill," *Int. J. Bifurcation Chaos* **22**, 1230012 (2012).
- ¹⁰G. Haller and A. C. Poje, "Finite time transport in aperiodic flows," *Physica D* **119**, 352–380 (1998).
- ¹¹A. C. Poje, G. Haller, and I. Mezić, "The geometry and statistics of mixing in aperiodic flows," *Phys. Fluids* **11**, 2963–2968 (1999).
- ¹²J. A. Jiménez Madrid and A. M. Mancho, "Distinguished trajectories in time dependent vector fields," *Chaos* **19**, 013111 (2009).
- ¹³M. R. Allhouse and J.-L. Thiffeault, "Detecting coherent structures using braids," *Physica D* **241**, 95–105 (2012).
- ¹⁴F. J. Beron-Vera, Y. Wang, M. J. Olascoaga, G. J. Goni, and G. Haller, "Objective detection of oceanic eddies and the Agulhas leakage," *J. Phys. Oceanogr.* **43**, 1426–1438 (2013).
- ¹⁵D. H. Kelley, M. R. Allhouse, and N. T. Ouellette, "Lagrangian coherent structures separate dynamically distinct regions in fluid flows," *Phys. Rev. E* **88**, 013017 (2013).
- ¹⁶G. Haller, "Lagrangian coherent structures," *Annu. Rev. Fluid Mech.* **47**, 137–161 (2015).
- ¹⁷G. Froyland and K. Padberg, "Almost-invariant sets and invariant manifolds—connecting probabilistic and geometric descriptions of coherent structures in flows," *Physica D* **238**, 1507–1523 (2009).
- ¹⁸G. Froyland, N. Santitissadeekorn, and A. Monahan, "Transport in time-dependent dynamical systems: Finite-time coherent sets," *Chaos* **20**, 043116 (2010).
- ¹⁹E. M. Boltt and N. Santitissadeekorn, *Applied and Computational Measurable Dynamics* (SIAM, 2013).
- ²⁰T. Ma and E. M. Boltt, "Relatively coherent sets as a hierarchical partition method," *Int. J. Bifurcation Chaos* **23**, 1330026 (2013).

- ²¹P. Tallapragada and S. D. Ross, "A set oriented definition of finite-time lyapunov exponents and coherent sets," *Commun. Nonlinear Sci. Numer. Simul.* **18**, 1106–1126 (2013).
- ²²G. Froyland and K. Padberg-Gehle, "Finite-time entropy: A probabilistic approach for measuring nonlinear stretching," *Physica D* **241**, 1612–1628 (2012).
- ²³T. Ma and E. Boltt, "Differential geometry perspective of shape coherence and curvature evolution by finite-time nonhyperbolic splitting," *Int. J. Bifurcations Chaos* (to be published).
- ²⁴T. Ma and E. Boltt, "Differential geometry perspective of shape coherence and curvature evolution by finite-time nonhyperbolic splitting," *SIAM J. Appl. Dyn. Syst.* **13**, 1106–1136 (2014).
- ²⁵R. L. Devaney, L. Devaney, and L. Devaney, *An introduction to Chaotic Dynamical Systems* (Addison-Wesley, Reading, 1989), Vol. 6.
- ²⁶R. C. Robinson, *An Introduction To Dynamical Systems: Continuous and Discrete* (American Mathematical Society, 2012), Vol. 19.
- ²⁷K. T. Alligood, T. D. Sauer, and J. A. Yorke, *Chaos* (Springer, 1996).
- ²⁸S. Smale, "Differentiable dynamical systems," *Bull. Am. Math. Soc.* **73**, 747–817 (1967).
- ²⁹B. Kitchens, *Symbolic Dynamics: One-Sided, Two-Sided and Countable State Markov Shifts* (Springer Science & Business Media, 1998).
- ³⁰C. Robinson, *Dynamical Systems: Stability, Symbolic Dynamics, and Chaos* (CRC Press, 1995).
- ³¹E. M. Boltt, T. Stanford, Y.-C. Lai, and K. Życzkowski, "What symbolic dynamics do we get with a misplaced partition? On the validity of threshold crossings analysis of chaotic time-series," *Physica D* **154**, 259–286 (2001).
- ³²R. Scorer, *Natural Aerodynamics: International Series of Monographs on Aeronautical Sciences and Space Flight: Aerodynamics* (Elsevier, 2014), Vol. 1.
- ³³P. A. Davidson, *Turbulence: An Introduction for Scientists and Engineers* (Oxford University Press, 2004).
- ³⁴L. Sirovich, "Chaotic dynamics of coherent structures," *Physica D* **37**, 126–145 (1989).
- ³⁵T. Theodorsen, "Mechanism of turbulence," in *Proceedings of the Midwestern Conference on Fluid Mechanics* (Ohio State University, Columbus, OH, 1952).
- ³⁶T. Theodorsen, "The structure of turbulence," in *50 Jahre Grenzschichtforschung*, edited by H. Görtler and W. Tollmein (1955).
- ³⁷E. M. Boltt, "Stability of order: An example of horseshoes 'near' a linear map," *Int. J. Bifurcation Chaos* **9**, 2081–2090 (1999).
- ³⁸T. Peacock and J. Dabiri, "Introduction to focus issue: Lagrangian coherent structures," *Chaos* **20**, 017501 (2010).
- ³⁹G. Haller, "Lagrangian coherent structures from approximate velocity data," *Phys. Fluids (1994-present)* **14**, 1851–1861 (2002).
- ⁴⁰S. C. Shadden, F. Lekien, and J. E. Marsden, "Definition and properties of Lagrangian coherent structures from finite-time Lyapunov exponents in two-dimensional aperiodic flows," *Physica D* **212**, 271–304 (2005).

- ⁴¹G. H. Golub and C. F. Van Loan, *Matrix Computations* (JHU Press, 2012), Vol. 3.
- ⁴²F. d'Ovidio, V. Fernández, E. Hernández-García, and C. López, "Mixing structures in the Mediterranean Sea from finite-size Lyapunov exponents," *Geophys. Res. Lett.* **31**, L17203, doi:10.1029/2004GL020328 (2004).
- ⁴³A. J. Mariano, A. Griffa, T. M. Özgökmen, and E. Zambianchi, "Lagrangian analysis and predictability of coastal and ocean dynamics 2000," *J. Atmos. Oceanic Technol.* **19**, 1114–1126 (2002).
- ⁴⁴R. Peikert, A. Pobitzer, F. Sadlo, and B. Schindler, "A comparison of finite-time and finite-size Lyapunov exponents," in *Topological Methods in Data Analysis and Visualization III*, edited by P.-T. Bremer, I. Hotz, V. Pascucci, and R. Peikert (Springer International Publishing, 2014), pp. 187–200.
- ⁴⁵M. do Carmo, *Differential Geometry of Curves and Surfaces Prentice-Hall International* (Englewood Cliffs, 1976).
- ⁴⁶G. Haller and F. Beron-Vera, "Coherent lagrangian vortices: The black holes of turbulence," *J. Fluid Mech.* **731**, R4 (2013).
- ⁴⁷G. Froyland, "Dynamic isoperimetry and the geometry of lagrangian coherent structures," e-print [arXiv.org/pdf/1411.7186](https://arxiv.org/pdf/1411.7186).
- ⁴⁸K. Menger, "Untersuchungen über eine allgemeine metrik. vierte untersuchung. zur metrik der liurven," *Math. Ann.* **103**, 467–501 (1932).
- ⁴⁹J. Leger, "Menger curvature and rectifiability," *Ann. Math.* **149**, 831–869 (1999).
- ⁵⁰S. F. M. Lambert, M. Surhone, and M. T. Timpledon, *Menger Curvature* (VDM Publishing, 2010).
- ⁵¹W. Press, B. Flannery, S. Teukolsky, and W. Vetterling, *Numerical Recipes in FORTRAN: The Art of Scientific Computing*, 2nd ed. (Cambridge University Press, 1992).
- ⁵²L. P. Eisenhart, *A Treatise on the Differential Geometry of Curves and Surfaces* (Ginn, 1909).
- ⁵³P. G. Tait, "Note on the circles of curvature of a plane curve," *Proc. Edinburgh Math. Soc.* **14**, 403 (1896).
- ⁵⁴D. H. Kelley and N. T. Ouellette, "Onset of three-dimensionality in electromagnetically forced thin-layer flows," *Phys. Fluids* **23**, 045103 (2011).
- ⁵⁵Y. Liao, D. H. Kelley, and N. T. Ouellette, "Effects of forcing geometry on two-dimensional weak turbulence," *Phys. Rev. E* **86**, 036306 (2012).
- ⁵⁶Y. Liao and N. T. Ouellette, "Spatial structure of spectral transport in two-dimensional flow," *J. Fluid Mech.* **725**, 281–298 (2013).
- ⁵⁷N. T. Ouellette, H. Xu, and E. Bodenschatz, "A quantitative study of three-dimensional Lagrangian particle tracking algorithms," *Exp. Fluids* **40**, 301–313 (2006).
- ⁵⁸N. Mordant, A. M. Crawford, and E. Bodenschatz, "Experimental Lagrangian probability density function measurement," *Physica D* **193**, 245–251 (2004).